THE JOURNAL OF BIOLOGICAL CHEMISTRY VOL. 290, NO. 40, pp. 24326–24339, October 2, 2015

Glutamate Transporter Homolog-based Model Predicts That Anion-π Interaction Is the Mechanism for the Voltage-dependent Response of Prestin*[S]

Received for publication, March 5, 2015, and in revised form, August 13, 2015 Published, JBC Papers in Press, August 17, 2015, DOI 10.1074/jbc.M115.649962

Sándor Lovas[1], **David Z. Z. He**[2], **Huizhan Liu, Jie Tang, Jason L. Pecka, Marcus P. D. Hatfield, and Kirk W. Beisel**[3]

From the Department of Biomedical Sciences, Creighton University School of Medicine, Omaha, Nebraska 68178

Background: The structure of the transmembrane domain of prestin and its mechanism of action are unknown.
Results: Glt_{Ph}-based model predicts that aromatic residues bind intracellular anions through anion-π interactions.
Conclusion: Aromatic residues in the proposed ion tunnel confer prestin with a unique capability to perform electromechanical conversions.
Significance: Anion-π interactions are identified as a novel mechanism to explain unique voltage-dependent property of prestin.

Prestin is the motor protein of cochlear outer hair cells. Its unique capability to perform direct, rapid, and reciprocal electromechanical conversion depends on membrane potential and interaction with intracellular anions. How prestin senses the voltage change and interacts with anions are still unknown. Our three-dimensional model of prestin using molecular dynamics simulations predicts that prestin contains eight transmembrane-spanning segments and two helical re-entry loops and that tyrosyl residues are the structural specialization of the molecule for the unique function of prestin. Using site-directed mutagenesis and electrophysiological techniques, we confirmed that residues Tyr^{367}, Tyr^{486}, Tyr^{501}, and Tyr^{508} contribute to anion binding, interacting with intracellular anions through novel anion-π interactions. Such weak interactions, sensitive to voltage and mechanical stimulation, confer prestin with a unique capability to perform electromechanical and mechano-electric conversions with exquisite sensitivity. This novel mechanism is completely different from all known mechanisms seen in ion channels, transporters, and motor proteins.

Mammalian hearing is extremely sensitive and exhibits exquisite frequency selectivity. The inner ear possesses an active process that can overcome the viscous damping and structural impedance imposed by the architecture and mechanical property of the organ of Corti. The electromotile property of cochlear outer hair cells, a mammalian cellular innovation, underlies this active amplification (1–4). The fundamental molecular basis of outer hair cell electromotility is the motor protein prestin (2, 5, 6). As a motor protein, prestin is unique in that its conformational change is dependent on voltage, and the speed of such change is in the microsecond range (7).

Prestin, encoded by the *Slc26A5* gene, is a functionally distinct member of the solute carrier 26 (SLC26A)[4] anion transporter protein family (8, 9). The overall tertiary structure of prestin consists of three domains: the N-terminal domain (~100 amino acid residues), a highly conserved central core of hydrophobic amino acids (~400 amino acid residues), and the C-terminal domain (~240 amino acid residues) (8). The N- and C-terminal domains are both located in the cytoplasmic side of the plasma membrane, whereas the hydrophobic core is embedded in the cell membrane. The sulfate transporter (SulTP) signature sequence is in the hydrophobic core, whereas the sulfate transporter and anti-σ factor antagonist (STAS) domain is in the C-terminal domain (10). Prestin can respond to voltage change (signified by the presence of a gating current) and undergo conformational change (reflected by length change of outer hair cells). Such voltage-dependent properties lie in distinct regions within the SulTP domain (residues 70–512) (11–14). Nevertheless, the underlying mechanism and the identity of residue(s) associated with the voltage sensor are still unresolved. Studies using site-directed mutagenesis and electrophysiology have suggested that intracellular anions, namely chloride and bicarbonate, serve as an extrinsic voltage sensor (6). The alternative view is that movement of charged residues modulated by chloride ions in an allosteric manner serves as a voltage sensor (15, 16). Nevertheless, the questions of which residues are the anion-binding residue(s) and how they interact with the anions are still controversial. Determination of the mechanism for voltage sensing and the residues for

* This work was supported, in whole or in part, by National Institutes of Health Grant R01 DC 004696 from the NIDCD (to D. Z. Z. H.). The authors declare that they have no conflicts of interest with the contents of this article.
[S] This article contains supplemental Data S1 and Movie S2.
[1] To whom correspondence may be addressed: Dept. of Biomedical Sciences, Creighton University School of Medicine, 2500 California Plaza, Omaha, NE 68178. Tel.: 402-280-5753; E-mail: slovas@creighton.edu.
[2] To whom correspondence may be addressed. E-mail: davidhe@creighton.edu.
[3] To whom correspondence may be addressed. E-mail: kirkbeisel@creighton.edu.

[4] The abbreviations used are: SLC, solute carrier; SulTP, sulfate transporter; STAS, sulfate transporter and anti-σ factor antagonist; APC, amino acid-polyamine-organocation; TM, transmembrane; MD, molecular dynamics; Glt_{Ph}, *P. horikoshii* glutamate symport protein; r.m.s.d., root mean square deviation; ECD, electronic circular dichroism; TFE, 2,2,2-trifluoroethanol; gPres, gerbil (*M. unguiculatus*) prestin; EGFP, enhanced GFP; ICF, intracellular finger; NLC, nonlinear capacitance; CLC, chloride-conducting; EL, extracellular loop; HP, helical pin; ACN, acetonitril.

interaction with anions is the key to understanding how prestin works.

The SLC26A family of anion transporters has been included as a distant member in the amino acid-polyamine-organocation (APC) superfamily (17–19). Saier and co-workers (19, 20) placed the sulfate permease family of transporters within the APC branch that includes the anion exchanger (SLC4), nucleobase-cation symporter-2 (SLC23), and benzoate transporter/permease transporters. This group of transporters represents the most distant and distinct branch of the APC superfamily with the sulfate permease transporter family representing an outlying cluster. Typically, the APC transporters display a 2-fold pseudosymmetrical topology consisting of four to seven transmembrane (TM)-spanning regions (19). The benzoate transporter/permease, anion exchanger 1, and nucleobase-cation symporter-2 transporters are furthermore unique within the APC superfamily hierarchy by exhibiting a 7-7 TM topology, which is supported by the available crystal structures for anion exchanger 1 (21) and UraA (22). On the basis of these data, it was suggested that sulfate permease transporters also should exhibit a 7-7 TM topology. Recently, the structure of UraA was used as a template to predict a model of the SulTP domain of prestin (23). The membrane topology of the model was validated by the substituted cysteine accessibility method. However, the UraA model does not appear to be able to explain the mechanism underlying the voltage sensing, anion binding, and piezoelectric property of prestin.

To circumvent the unavailability of x-ray crystallography data for prestin, we used a combination of computational folding recognition, homology modeling, and molecular dynamics (MD) simulations to determine the three-dimensional structure of the SulTP domain. Our computational model suggested that prestin has structural similarity to the *Pyrococcus horikoshii* glutamate symport protein (Glt_{Ph}) (10, 24). Specific residues within the internal anion binding site (residues Tyr^{367} and Tyr^{486}) and adjacent to the intracellular tunnel entrance (residues Tyr^{501} and Tyr^{508}) participate in the voltage sensor mechanism of prestin. The non-covalent anion-π interactions (25–28) of anions with the aromatic rings of Tyr^{367}, Tyr^{486}, Tyr^{501}, and Tyr^{508} furnish prestin with a unique capability to bind to anions and respond to voltage and mechanical stimulations.

Experimental Procedures

Fold Prediction and Homology Modeling of Prestin—Appropriate templates for the three-dimensional structural determination of the SulTP domain (residues 70–512) of prestin were selected by submitting eutherian orthologs from rat, gerbil, and human and a consensus eutherian sequence (29) to the pGenTHREADER profile-based fold recognition program (30).

Homology models were built using the YASARA software package (31). For all modeling, the hm_build.mcr macro of the YASARA package was used with the following parameters: modeling speed, slow; number of PSI-BLAST iterations in template search, 6; maximum allowed PSI-BLAST E-value to consider template, 0.5; maximum number of templates to be used, 5; maximum number of templates with same sequence, 1; maximum oligomerization state, 1; maximum number of alignment variations per template, 5; maximum number of conformations tried per loop, 100; and maximum number of residues added to the termini, 10. The homology modeling procedure only included energy minimizations of structures in water; therefore, the resultant structures were further refined. The models were embedded in a phosphatidylethanolamine lipid bilayer, solvated with water molecules, and submitted to 1-ns MD simulation using the md_runmembrane.mcr macro of YASARA.

MD Simulation—The final homology model was submitted to three independent 100-ns MD simulations with the DESMOND molecular dynamics package (32) using the OPLS-AA/L force field (33). *N*-Acetyl and *N*-methylamide protecting groups were added to the N and C termini, respectively, to preserve the electronic structure of the backbone as in prestin. The protein was embedded in a lipid bilayer composed of 142 1-palmitoyl-2-oleoylphosphatidylcholine molecules and solvated with 15,713 SPC water molecules. The net charges were neutralized with Cl^- ions. The structure of the system first was relaxed by using the MultiSim script of DESMOND that includes a series of energy minimizations and short MD simulations. The system was then equilibrated with 1-ns NPT, constant number of molecules, constant pressure (1 bar), and constant temperature (310 K) simulation. The pressure and temperature were kept constant with a Berendsen barostat (relaxation time, 2 ps) and thermostat (relaxation time, 1 ps), respectively. For short range non-bonded interactions, a 9-Å cutoff was used, and the long range electrostatic interaction was treated with the smooth particle mesh Ewald method. The equation of motion was integrated with the multistep RESPA scheme (34) with time steps of 2, 2, and 6 fs for the bonded, short range, and long range non-bonded interactions, respectively. Bonds involving H-atoms were constrained to their equilibrial values with the SHAKE method (35). For the production simulations (100 ns), the same parameters were used. Using Visual Molecular Dynamics (VMD), trajectories were converted to GROMACS (36) format and analyzed with the GROMACS analysis software suite. Cluster analyses of the trajectories were performed by the GROMOS method of clustering (37) using a backbone root mean square deviation (r.m.s.d.) cutoff of 0.15 nm. Secondary structural changes during simulations were determined by using the Dictionary of Secondary Structure of Proteins (DSSP) program (38).

Peptide Synthesis and Purification—To preserve the electronic structure of the backbone as in the whole protein, the fragments were synthesized as N-terminal acetyl- and C-terminal amide-protected peptides. The syntheses were performed on a CEM Liberty Microwave peptide synthesizer (CEM Corp., Matthews, NC) at a 0.1-mmol scale using Rink amide aminomethyl resin and a 5 M excess of N^{α}-Fmoc (*N*-(9-fluorenyl)methoxycarbonyl)-protected amino acids as described previously (39).

Electronic Circular Dichroism (ECD) Spectropolarimetry—ECD spectra of peptides were recorded using a Jasco J-810 spectropolarimeter. ECD spectra were obtained by averaging 20 scans from 185 to 250 nm at 100 nm/min. The peptides were dissolved either in 20 mM KH_2PO_4 buffer (pH 7), 50% 2,2,2-trifluoroethanol (TFE) in the same buffer (v/v), or 100% TFE, and their spectra were measured in a quartz cell with a 0.05-cm path length. The TM8 fragment of prestin was only soluble in

80% acetonitrile (ACN). The ECD spectra of the peptides were measured at peptide concentrations of 25, 50, and 100 μM to ensure that the peptide concentration did not affect the shape of the spectrum. The solutions were kept at 4 °C with a Jasco PFD-425 single position Peltier thermostated cell holder. Background spectra of the solvents were subtracted. Mean residue molar ellipticities were calculated using peptide concentrations determined by quantitative reverse phase HPLC (40). To determine the secondary structure content of peptides, CDSSTR analysis (41) was performed with data set 6 using the DichroWeb website (42).

Prestin Constructs, Site-directed Mutagenesis, and Expression—Gerbil (*Meriones unguiculatus*) prestin (gPres) cDNA was cloned into the pEGFP-N1 vector (p-gPres-eGFP) to generate the C-terminal EGFP fusion proteins. Mutated gerbil SLC26A5 cDNAs were produced by site-directed mutagenesis to generate EGFP fusion proteins as described previously (14). To create an intracellular finger (ICF)-truncated prestin, a minigene was synthesized (CCACCGGTGTTCGGCCTGTACTCTTCATTTTATCCTGTTATCATGTACTGTTTCTTTGGGACCTCCAGACACATATCTATAGGTCCTTTCGCCGGTGGTCCCGATGACATCGTCATCCCGGGAGGAGTGAACGCAACCAACGGCACGGAGGCCCGAGACGCGCTGAGAGTGAAAGTCGCCATGTCTGTCACCCTGCTCTCAGGAATCATTCAGTTTTGCCTAGGTGTGTGCAGGTTTGGATTTGTGGCCATATACCTCACGGAGCCGCTGGTGCGAGGGTTCACCACCGCCGCCGCCGTGCACGTCTTC with the deduced peptide sequence of PVFGLYSSFYPVIMYCFFGTSRHISIGPFAGGPDDIVIPGGVNATNGTEARDALRVKVAMSVTLLSGIIQFCLGVCRFGFVAIYLTEPLVRGFTTAAAV) and inserted into pIDTSmart-Kan (Integrated DNA Technologies, Coralville, IA). This fragment was excised using AgeI/BtrI and ligated into a prepared p-gPres-eGFP plasmid using a BtrI/partial BsaWI digestion. The correct orientation, reading frame, and amino acid composition of all the constructs were confirmed by DNA sequence analyses.

Cell Culture and Transient Transfection—Human embryonic kidney (HEK) cells were cultured in DMEM solution (Invitrogen) supplemented with 10% fetal bovine serum. Prestin or mutants (4 μg) were introduced into the dishes using 10 μl of Lipofectamine (Invitrogen) following the protocol from the manufacturer.

Confocal Imaging—Membrane-associated expression of prestin mutations was verified 24 h after transfection by confocal imaging performed on an LSM 510 microscope (Zeiss, Thornwood, New York, NY) using a 40× water immersion objective.

Electrophysiology—Nonlinear capacitance (NLC) measurements using whole cell voltage clamp techniques were performed 24–48 h after transfection on cells with robust membrane-associated EGFP expression. During electrophysiological recordings, cells were bathed in an extracellular solution containing 120 mM NaCl, 2 mM $MgCl_2$, 2 mM $CoCl_2$, 20 mM triethanolamine, 10 mM HEPES, and 10 mM 4-aminopyridine. Recording pipettes were pulled from borosilicate glass with resistances between 2.5 and 5.0 megaohms and filled with a solution containing 140 mM CsCl, 2 mM $MgCl_2$, 10 mM EGTA, and 10 mM HEPES. Membrane capacitance was measured using a two-sine wave voltage stimulus protocol (10-mV peak at both 390.6 and 781.2 Hz) with subsequent fast Fourier transform-based admittance analysis (43) from a holding potential of 0 mV. The capacitive currents were sampled at 100 kHz and low pass-filtered at 5 kHz. Series resistance was compensated offline. The capacitive currents were amplified by Axopatch 200B (Molecular Devices, Sunnyvale, CA). Data were acquired using jClamp (Scisoft, New Haven, CT) and analyzed with Igor (WaveMetrics, Portland, OR).

The NLC can be described as the first derivative of a two-state Boltzmann function relating nonlinear charge movement to voltage (44, 45). The capacitance function is described as follows.

$$C_m = C_{\text{lin}} + \frac{Q_{\text{max}}\alpha}{\exp[\alpha(V_m - V_{1/2})](1 + \exp[-\alpha(V_m - V_{1/2})])^2} \quad \text{(Eq. 1)}$$

where Q_{max} is maximum charge transfer, $V_{1/2}$ is the voltage at which the maximum charge is equally distributed across the membrane or equivalently the peak of the voltage-dependent capacitance, C_{lin} is linear capacitance, and $\alpha = ze/kT$ is the slope of the voltage dependence of charge transfer where k is the Boltzmann constant, T is absolute temperature, z is the valence of charge movement, and e is electron charge. The Q_{max} was normalized by C_{lin} in the results. The C_{lin} is proportional to the surface area of the membrane (the size of the cell). Because C_{lin} is not relevant to this study, we subtracted the linear capacitance and only presented the NLC as a function of voltage for the data presented under "Results." To compare the magnitude of NLC obtained from different cells with different sizes, we normalized the NLC by C_{lin}. Data were collected from cells with membrane resistance greater than 500 megaohms after rupturing and exhibiting normal membrane capacitance (C_m) and resistance (R_m) values. Series resistance was compensated offline. For each construct, NLC data were acquired from cells representing at least four separate transfection experiments. Data were analyzed with Student's t test, and significance was considered at $p < 0.05$.

Results

Homology Modeling of the SulTP Domain of Prestin

Nine different structures primarily consisting of three groups of proteins with a highly significant fold characteristic similar to the SulTP domain (residues 70–512) of prestin ($p < 0.001$) were identified with the pGenTHREADER three-dimensional fold recognition method (30). The first group represented proteins with a solenoid protein domain and included human cullin-1 ligase (Protein Data Bank code 1U6G), *Saccharomyces cerevisiae* exportin Cse1p (Protein Data Bank code 1WA5), rat clathrin-associated adaptor protein (Protein Data Bank code 2VGL), and human exportin-5 (Protein Data Bank code 3A6P). The solenoid domain most closely resembles the topological models of prestin with the up and down α-helical membrane-spanning motifs (6, 46). The next group consisted of two chloride-conducting (CLC) chloride channel proteins, the *Salmonella enterica* serovar Typhimurium CLC chloride channel

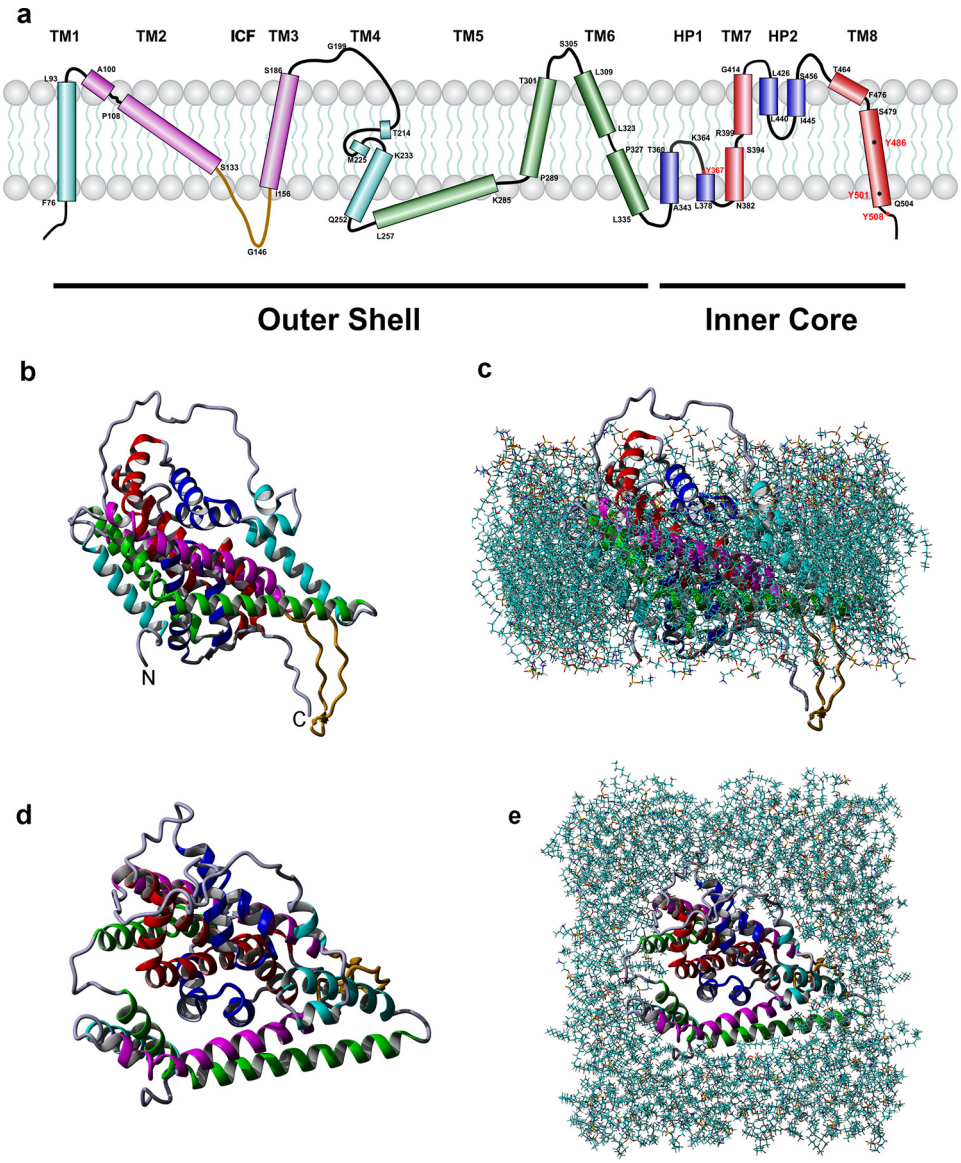

FIGURE 1. **Structural model of prestin.** *a*, schematic representation of the three-dimensional structure of the SulTP domain of prestin. *Cylinders* represent TM helices, and loops are indicated by *black lines*. The major structural features (outer shell and the inner core) are indicated at the *bottom* of the panel. The color of the different TM helices, ICF, HP1, and HP2 correspond to the coloring scheme of *b*–*e*. Lipid molecules are represented by *gray spheres* and *lines*. At the *top* is the extracellular region. *b*, side view of the ribbon representation of the three-dimensional structure of the SulTP domain of prestin. At the *top* is the extracellular region. *N* and *C* indicate the N- and C-terminal ends, respectively, of prestin. The ICF is *yellow*-colored. *c*, side view of 1-palmitoyl-2-oleoylphosphatidylcholine lipid bilayer-embedded prestin. The *top* is the extracellular region. *d*, extracellular view of prestin. *e*, extracellular view of 1-palmitoyl-2-oleoylphosphatidylcholine lipid bilayer-embedded prestin.

(CLCst) (Protein Data Bank code 1KPL) and the *Escherichia coli* CLC chloride channel (CLC-ec1) (Protein Data Bank code 1OTS). The third group represented five different transporter proteins. These were the Glt_{Ph} sodium-dependent aspartate transporter (Protein Data Bank code 2NWL), the *P. horikoshii* proton-glutamate symport protein (Protein Data Bank code 1XFH), the *Microbacterium liquefaciens* nucleobase-cation symport-1 (Protein Data Bank code 2JLN), the *Aquifex aeolicus* Na^+/Cl^--dependent transporter (LeuT) (Protein Data Bank code 3F3A), and the *Vibrio parahaemolyticus* sodium/galactose symporter (vSGLT) (Protein Data Bank code 3DH4). The bovine cytochrome *c* oxidase polypeptide I (Protein Data Bank code 1V54) also exhibited a highly significant folding pattern similar to that of prestin. However, for our subsequent analyses, it was selected as a functionally dissimilar protein.

Using YASARA (31), SLC26A5 ortholog and paralog sequences from different species (zebrafish, chicken, opossum, gerbil, and rat) were examined for fold similarities with the above nine proteins. Attempts to model prestin paralogs and orthologs using only the CLC-ec1 structure as a template (47) did not yield any viable structural models; therefore, from the above three groups of proteins, nine templates (1WA5, 1KPL, 1OTS, 2NWL, 1XFH, 2JNL, 3F3A, 3DH4, and 1V54) were selected to obtain hybrid models of prestins. Of these templates, 1V54 and 1WA5 never had significant alignments with prestin and were discarded. The hybrid models that were built on the other seven templates had better Z-scores (−2.217) than those of the individually built models. Furthermore, rat prestin had the best Z-score (−2.014) using Glt_{Ph} (2NWL) as a template. Although the overall sequence identity between the

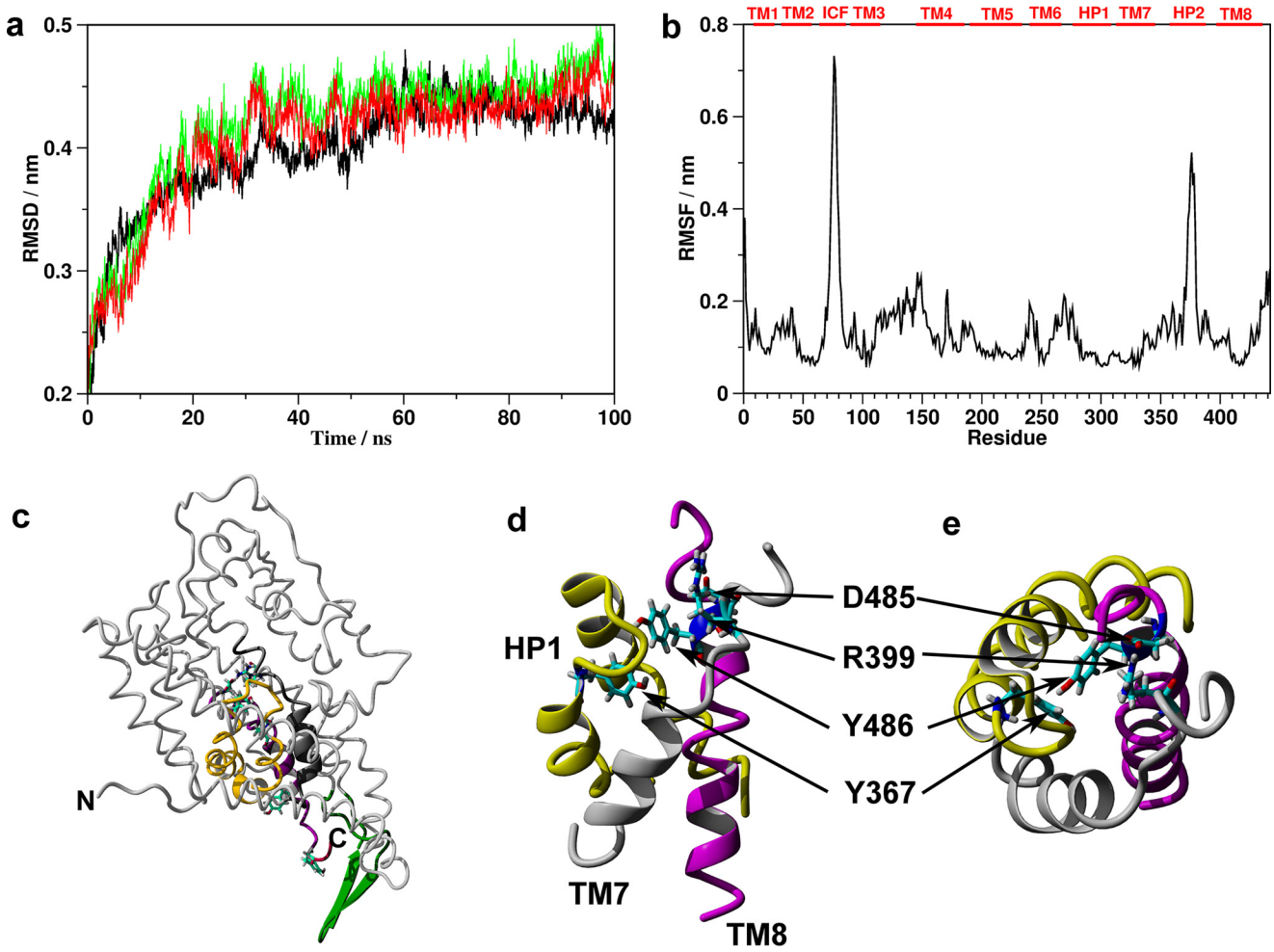

FIGURE 2. **Molecular dynamics characterization of prestin.** *a*, evolution of r.m.s.d. of the backbone atoms from the starting structure during three independent MD simulations. Simulation 1, *black*; simulation 2, *green*; simulation 3, *red*. *b*, root mean square fluctuation (*RMSF*) of residue positions. Major structural elements are designated by *red bars* on the *upper y axis*. *c*, tube representation of the central structure of the largest cluster of simulation 1. Regions of the inner core that form the proposed tunnel are color-coded as follows: HP1, *yellow*; TM7, *dark gray*; TM8, *pink*; ICF, *green*. The β-hairpin structure is indicated by *arrows*. *N* and *C* indicate the N- and C-terminal ends, respectively, of prestin. *d* and *e*, close-up of the tunnel in side- and top-down views, respectively. The color codes used are the same as in *c*. Interacting residues of the tunnel are shown in *stick* and indicated by *black arrows*.

SulTP domain of prestin and the Glt_{Ph} protein is 13.1%, the three-dimensional structure of the protein is more conserved than the sequence (48, 49). Therefore, our final homology model of the rat prestin (Fig. 1) was created by using four x-ray structures (2NWL, 2NWW, 2NWX, and 1XFH) of Glt_{Ph} with a satisfactory Z-score of −1.837. The major structural features of the model are eight TM-spanning domains, TM3-TM4 extracellular loop (EL3-4), two helical pin (HP) re-entry loops, and the ICF, the loop that connects TM2 and TM3 (Fig. 1*a* and supplemental Data S1). The overall structure can be further divided into an outer shell represented by TM1–TM6 and an inner core (HP1, HP2, TM7, TM8, and ICF) that contain the putative transport-associated and anion-sensing features of prestin.

MD Simulations

To validate and refine the Glt_{Ph}-like structure of the SulTP domain of rat prestin, we performed three independent 100-ns MD simulations in an aqueous lipid-membrane environment. The structural stability of prestin was evaluated by calculating the r.m.s.d. of the backbone atoms from the starting structure along the trajectories (Fig. 2*a*). During an initial 40 ns of each of the three simulations, the structure of prestin modestly deviated from that of the initial homology model-based structure, and r.m.s.d. values reached equilibrium with fluctuation around an average value. These deviations from the initial homology model-based structure, however, did not result in substantial structural reorganization. All three simulations resulted in similar structural features; thus we show our results from simulation 1. Per residue root mean square fluctuations (RMSF) from the mean positions of individual Cα atoms showed that the largest motions took place at ICF and HP2 (Fig. 2*b*). ICF and its movement are unique to our proposed prestin model. A similar large motion was detected at HP2 and is comparable with that in the structural template Glt_{Ph} protein (50), indicating similar dynamic properties. Cluster analysis of the trajectories generated 19, 30, and 18 clusters for simulations 1, 2, and 3, and the largest cluster contained 58.2, 29.5, and 58.5% of all sampled structures, respectively. The relatively high portion of structures in the largest cluster of two trajectories further indicates that prestin forms a stable structure. Fig. 2*c* shows the central structure of the largest cluster from simula-

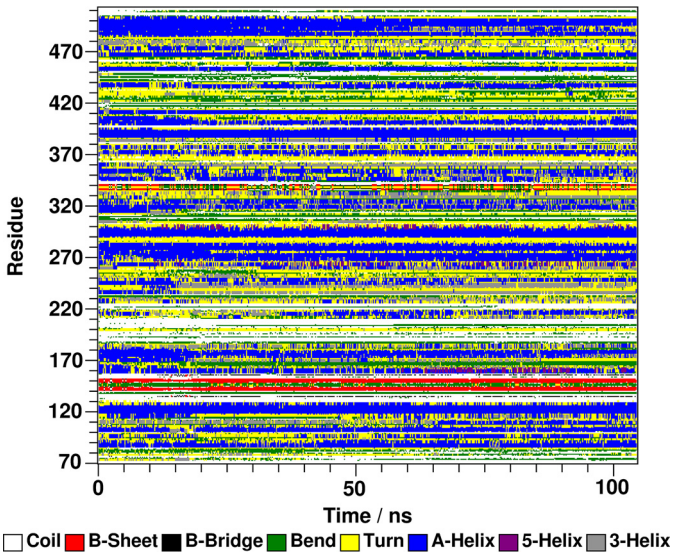

FIGURE 3. **Change in secondary structure during MD simulation of the structure of prestin.** Secondary structure content was determined using the Dictionary of Secondary Structure of Proteins (DSSP) method.

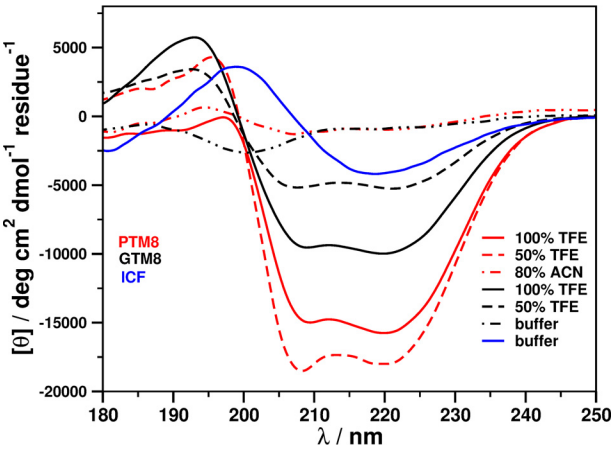

FIGURE 4. **The ECD spectra of 50 μM peptide fragments in different solutions.** PTM8 (*red*), residues Ser^{478}–Arg^{502} of prestin; GTM8 (*black*), residues Gly^{388}–Glu^{418} of Glt$_{Ph}$; ICF (*blue*), residues Ser^{133}–Ile^{156} of prestin. *deg*, degrees.

tion 1. Using YASARA, this structure was spatially aligned with chain A of the 1XFH template and had 2.136-Å backbone r.m.s.d. over 203 aligned residues (see supplemental Movie S2). In addition to a stable overall structure, a stable β-hairpin structure was formed by residues Ile^{140}–Val^{152} of the ICF (Fig. 2*c* and Fig. 3). To show that the β-hairpin formation was not a computational artifact, we chemically synthesized the Ser^{133}–Ile^{156} fragment of prestin and used ECD spectropolarimetry to explore its conformation. ECD measurements confirmed that ICF forms a β-sheet conformation in an aqueous buffer (Fig. 4 and Table 1).

Intramolecular Interactions Play Role in Chloride Ion Sensing

In the Glt$_{Ph}$ protein, the inner core forms a channel for substrate binding and translocation (50). We propose that, in a similar fashion, residues within the inner core of prestin play an important role for interaction with anions. Close scrutiny of the MD trajectories revealed that either invariant residues in the eutherian orthologs or conserved residues within the eutherian prestins contribute to the overall stability of the inner core and could provide a unique structural framework for sensing intracellular chloride ions. We observed three different types of interactions (Table 2): ionic, hydrogen bonding, and weakly polar interactions (51). The latter includes aromatic-aromatic (π-π) interactions between side chains of aromatic amino acids, π-backbone (π-bb) interactions between aromatic side chains and peptide backbone, and π-CH interactions between aromatic side chains and CH groups of side chains. Ionic interactions Lys^{77}-Glu^{374}, Arg^{197}-Glu^{468}, Lys^{283}-Glu^{374}, and Lys^{449}-Glu^{207} (Fig. 5) stabilize the structure of the inner core, whereas Arg^{399}-Asp^{485} ionic interaction (Figs. 2, *d* and *e*, and 6*a*) positions the side chain of Arg^{399} so that the $^{\delta}CH_2$ group interacts with the aromatic side chain of Tyr^{486} through π-CH interaction with 0.4-nm average distance between them (52) (Figs. 2, *d* and *e*, and 6*f*). In turn, the location of the aromatic side chain of Tyr^{486} is stabilized in space so that it interacts with the aromatic side chain of Tyr^{367} though a π-π interaction (Figs. 2, *d* and *e*, and 6, *b* and *c*). The distance between the center of the two aromatic rings and the angle between the planes of the two aromatic rings are around 0.4 nm and 110°, respectively, which are in agreement with x-ray protein structures in the Protein Data Bank (53). Residue Tyr^{501} of TM8 is located at the intracellular tunnel entrance of the inner core tunnel and interacts with the peptide backbone of residues Gly^{379}–Ile^{388} through a π-bb interaction (Figs. 6*e* and 7*a*). These residues connect HP1 and TM7. Residue Tyr^{508} of the intracellular tail interacts with several hydrophobic residues of the ICF through π-CH interactions (Table 2 and Fig. 6, *g*–*i*).

Data mining of the Protein Data Bank for anion-π interactions involving aromatic side chains of amino acid residues and inorganic anions such as Cl^-, Br^-, PO_4^{3-}, and NO_3^- revealed that Cl^- ion interacted most frequently among the anions (28). Furthermore, Cl^- was in close contact with His, Tyr, Phe, and Trp residues, respectively, in decreasing order of frequency. Energetic and electron density analysis showed that the interaction is weak, and nearby polar, charged, and H-bond-donating residues may enhance the interactions (26). Tyrosyl residues of HP1 and TM8 are located inside of our proposed tunnel (Fig. 7) so they can attract Cl^- ions and facilitate the ion movement into and within the tunnel.

Experimental Validation of Structure

ECD Spectropolarimetry—To experimentally validate our structural model, we selected the TM8 fragment (residues Ser^{478}–Arg^{502}) of the inner core of prestin (Fig. 1*a*) for chemical synthesis and subsequent structural analysis by ECD spectropolarimetry. In the Glt$_{Ph}$ structural template, residues of TM8 play an important role for substrate binding (50). We hypothesized that similar features might exist for prestin. As a control, we also synthesized the Gly^{388}–Glu^{418} TM8 fragment of Glt$_{Ph}$. As a transmembrane segment, TM8 fragment of prestin was hydrophobic, and we were not able to measure its ECD spectrum in an aqueous buffer but were able to measure its ECD spectrum in 80% acetonitrile. The ECD spectra were also determined in 50 and 100% TFE. Using organic solvents other than a strictly aqueous buffer can be justified by the fact that the peptide fragments are out of context with the rest of the protein and

TABLE 1
CDSSTR analysis of the ECD spectra of fragments of prestin and Glt_{Ph}

Peptide	Solution	Percentage of secondary structure			
		Helix	Sheet	Turn	Unordered
ICF[a]	Buffer	3	39	21	37
PTM8[b]	80% ACN	7	70	1	25
	50% TFE	49	23	11	16
	100% TFE	42	26	13	19
GTM8[c]	Buffer	3	26	45	27
	50% TFE	8	30	18	43
	100% TFE	21	21	18	40

[a] Ser^{133}–Ile^{156} fragment of prestin.
[b] Ser^{478}–Arg^{502} fragment of prestin.
[c] Gly^{388}–Glu^{418} fragment of Glt_{Ph}.

TABLE 2
Non-bonded interactions of the inner core of prestin
Red-colored residues are invariant within the eutherian orthologs, whereas the black-colored residues are conserved only in eutherian prestins. The location of a residue in prestin is given in parenthesis.

Type of Interaction[a]	Residues	
Ionic	K77 (TM1)	E374 (HP1)[b]
	R197 (L3-4)	E468 (TM8)
	K283 (TM5)	E374 (HP1)[b]
	R399 (TM7)	D485 (TM8)
	K449 (HP2)	E207 (EL3-4)
H-bonds	S133 (ICF)	S383 (TM7)[c]
π – π	Y367 (HP1)	Y486 (TM8)
π - bb	Y501 (TM8)	G379-I380[d]
π-CH	Y486 (TM8)	R399 (TM7)
	Y508 (TM8)	I140 (ICF)
	Y508 (TM8)	L142 (ICF)
	Y508 (TM8)	I144 (ICF)
	Y508 (TM8)	V147 (ICF)
	Y508 (TM8)	V149 (ICF)
	Y508 (TM8)	L151 (ICF)

[a] Types of interactions: π-π, between side chains of aromatic amino acids; π-bb, between aromatic side chains and peptide backbone; π-CH, between aromatic side chains and CH groups of side chains.
[b] HP1 does not move.
[c] Backbone - backbone and side chain - backbone hydrogen bonds.
[d] Peptide bond between the two residues.

its membranous environment. Therefore, it is possible that helical structures will not form spontaneously in an aqueous buffer system. Thus, it is a common practice to use the secondary structure-promoting agent TFE in ECD measurements (54). The weak signal of the prestin TM8 fragment in 80% acetonitrile solution could be attributed to either a β-sheet or an aggregated structure (Fig. 4). Increasing the TFE concentration induced an α-helical conformation in both prestin and Glt_{Ph} TM8 fragments (Fig. 4 and Table 1). The increasing α-helical conformation is consistent with structural properties of many well characterized fragments of different transmembrane proteins and indicates the correct structural assignment for TM8 in prestin.

Site-directed Mutagenesis and Electrophysiology—We examined the proposed structure of prestin with site-directed mutagenesis and electrophysiological measurement from HEK cells transfected with different sets of mutant prestin. Membrane expression of the mutant prestins was examined by confocal microscopy. A unique feature of our prestin model is ICF (residues Ser^{133}–Ile^{156}), which extends into the intracellular region and forms an antiparallel β-sheet conformation (Figs. 2*c* and 3). Because ICF is outside the TM-spanning structure of prestin, we assumed that prestin can still fold into a SulTP structure without ICF. Therefore, we expressed a variant of prestin in which residues Ser^{133}–Ile^{156} were replaced by a Gly-Gly dipeptide. Robust membrane expression of the mutant protein in HEK cells was detected 24 h after transfection as shown in Fig. 8*a*. Thus, it appeared that deletion of 23 amino acid residues of the ICF did not affect membrane targeting of the truncated protein. To determine whether deletion of ICF would affect prestin function, we measured NLC from HEK cells transfected by the mutant prestin. Wild-type gPres was used as a control. NLC, reflecting voltage-dependent charge movement arising from the redistribution of charged "voltage sensors" across the membrane, is usually used to describe the voltage-dependent characteristics of prestin. NLC is characterized by a bell-shaped dependence on membrane potential with a peak between −80 and −0 mV (44, 45). Fig. 8*a* shows NLC responses measured from HEK cells transfected by gPres ($n = 12$) and ICF-truncated prestin ($n = 8$). As shown, gPres exhibits a robust bell-shaped dependence on membrane potential with a peak capacitance close to 9% of the total membrane capacitance near −73 mV. We obtained two parameters ($V_{1/2}$ and z value) from nonlinear curve fitting of the NLC response using the first derivative of the Boltzmann function (Fig. 4*b*). $V_{1/2}$ is the voltage at which half of the total charges are translocated across the membrane, and z is the valence of charge movement. These two parameters are often used to define the magnitude and voltage dependence of NLC (44, 45). Curve fitting of normalized NLC of gPres yielded a $V_{1/2}$ value of -76.5 ± 5.3 mV and a z value of 0.74 ± 0.09. These numerical values are consistent with those reported in previous studies (5, 6, 16). In contrast, the NLC response of the truncated prestin was substantially reduced with a z value of 0.39 ± 0.09, which is significantly less than that of gPres ($p < 0.01$). The peak of NLC was also shifted toward depolarization with a $V_{1/2}$ value of -32 ± 5.3 mV. Taken together, these results suggest that, although deletion of ICF did not affect protein folding and membrane targeting, its voltage-dependent capability was significantly reduced but not completely eliminated, indicating the functional role of ICF.

The four tyrosyl residues (Tyr^{367}, Tyr^{486}, Tyr^{501}, and Tyr^{508}) of HP1 and TM8 are the putative anion-binding residues of prestin. Consequently, their modification might affect the NLC properties of prestin. We substituted these residues with either Ala, Arg, Phe, or Trp. We first measured NLC from HEK cells transfected with plasmids with substitution of Tyr^{367} and Tyr^{486} with either Ala, Arg, or Phe. These residues, which are

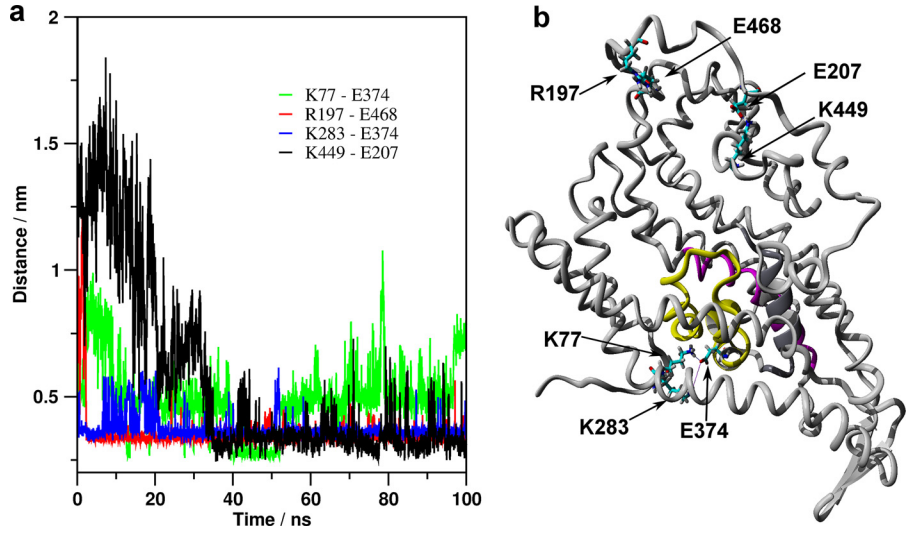

FIGURE 5. **Ionic interactions between positively and negatively charged side chains.** *a*, the distance between center of masses of either the -$^{\epsilon}NH_3^+$ group of lysine or -$^{\delta}NHC(NH_2)_2^+$ group of arginine and the -$^{\gamma}COO^-$ of glutamate during the MD simulation. Ionic interactions were considered when the distances between two oppositely charged groups were ≤0.5 nm. *b*, interacting residues in *a* are in *stick* and indicated by *arrows* in the tube representation of the central structure of the largest cluster of simulation 1.

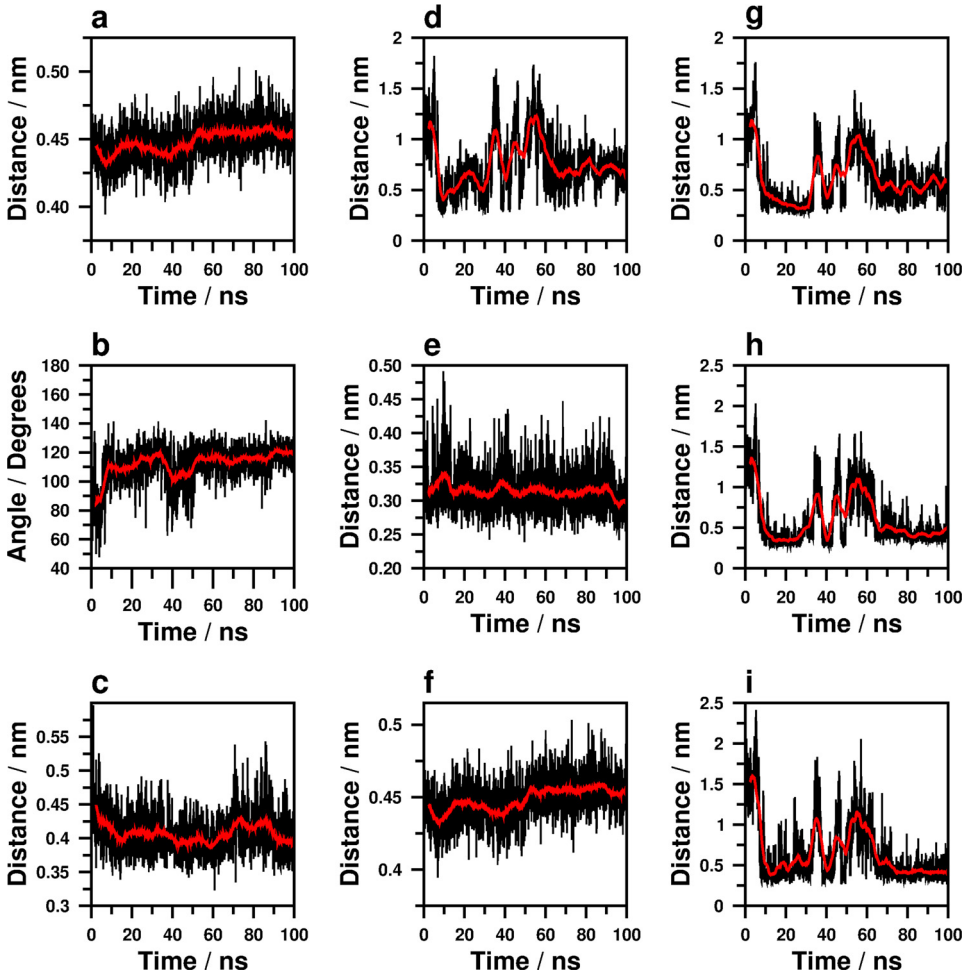

FIGURE 6. **Interactions between various functional groups of amino acid residues in prestin during MD simulation.** The interactions were assigned when distances and angles were in agreement with reported values in the literature (see Refs. 52, 53). *Red lines* are running averages at every 5-ns interval. *a*, distance between center of masses of the -$^{\delta}NHC(NH_2)_2^+$ group of Arg^{399} and the -$^{\beta}COO^-$ of Asp^{485}. *b*, angle between the planes of aromatic rings of Tyr^{367} and Tyr^{486}; planes of the aromatic rings were assigned as a plane formed by the Cγ, Cϵ1, and Cϵ2 atoms. *c*, distance between the center of mass of the aromatic rings of Tyr^{367} and Tyr^{486}. *d*, distance between center of masses of the aromatic ring of Tyr^{508} and the -$^{\delta}CH_2$ group of Leu^{142}. *e*, distance between center of masses of the aromatic ring of Tyr^{501} and the peptide bond between Gly^{379} and Ile^{380}. *f*, distance between center of masses of the aromatic ring of Tyr^{486} and the -$^{\delta}CH_2$ group of Arg^{399}. *g*, distance between center of masses of the aromatic ring of Tyr^{508} and the -$^{\delta}CH_2$ group of Leu^{151}. *h*, distance between center of masses of the aromatic ring of Tyr^{508} and the -$^{\gamma 1}CH_3$ and -$^{\gamma 2}CH_3$ groups of Val^{149}. *i*, distance between center of masses of the aromatic ring of Tyr^{508} and the -$^{\delta}CH_3$ group of Ile^{144}.

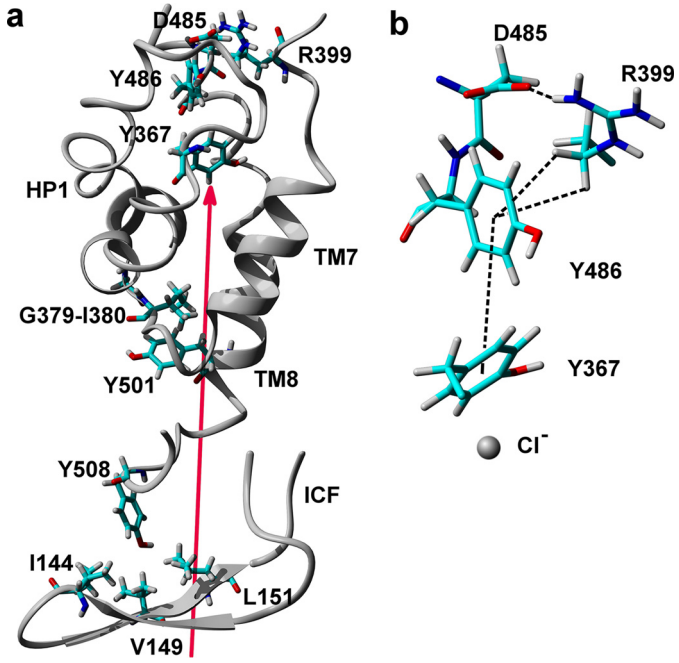

FIGURE 7. **Structure of the chloride sensor of prestin.** *a*, the backbone structure of the sensor is shown in *gray ribbon*, and the individual residues of HP1, TM7, TM8, and ICF that make up the chloride sensor are shown in *stick*. The *red arrow* indicates a possible path of chloride ions in the tunnel. *b*, stick representation of residues at the top of the channel. *Dashed lines* indicate the interactions between side chains of the following residues: Asp^{485}-Arg^{399}, ionic interaction; $^{\delta}CH_2$ of Arg^{399}-aromatic side chain of Tyr^{486}, CH-π interaction; aromatic side chain of Tyr^{486}-aromatic side chain of Tyr^{367}, π-π interaction. The *gray sphere* indicates a possible location of the Cl^- ion in the binding site.

located at the top of the tunnel, are part of the internal anion binding site in our model (Fig. 7). As shown in Fig. 8*b*, the magnitude of NLC was significantly reduced after either Tyr^{367} or Tyr^{486} was replaced by either Ala, Arg, or Phe. This is reflected by a significant reduction of the *z* value for all mutant prestins. The values of *z* and $V_{1/2}$ ($n = 8$ for each mutation) are presented in Fig. 8*b*. Furthermore, either Y367A or Y367R mutation resulted in almost complete elimination of the NLC, indicating a more significant role of Tyr^{367} in binding to Cl^- ion.

As part of the proposed internal anion binding site, Tyr^{501} and Tyr^{508} are located at the intracellular tunnel entrance (Fig. 7*a*). These residues were substituted with either Ala, Arg, Phe, or Trp, and the NLC responses of the mutant prestins were recorded. As shown in Fig. 9, *a* and *b*, mutations of either of these two residues resulted in a significant reduction of NLC and the *z* values. The more negative $V_{1/2}$ values for Y501R and Y508R mutants indicate that the arginyl residue binds the Cl^- ion more strongly than other residues, resulting in a decreased *z* value. We also did double mutations of these two residues with substitution by Phe or Trp. As shown in Fig. 9*c*, double mutations also caused a significant reduction of the NLC response and *z* value.

Discussion

In the present study, a predictive three-dimensional model of the SulTP domain of rat prestin was built using x-ray structures of the Glt_{Ph} protein as templates for homology modeling. The structural properties of the model were validated with subsequent MD simulations. On the basis of MD simulations, site-directed mutagenesis, and electrophysiological measurements, we propose a novel mechanism for the unique voltage-dependent function of prestin. Our results indicate that the aromatic side chains of the four tyrosyl residues (Tyr^{367}, Tyr^{486}, Tyr^{501}, and Tyr^{508}) form non-covalent bonds with intracellular anions through anion-π interactions. In this model, anions in the tunnel form non-covalent bonds with the aromatic side chains inside the tunnel at the resting condition (Fig. 10). Depolarizing voltage drives Cl^- ions toward the cytosol and disrupts the binding. Translocation of the anions and uncoupling of the non-covalent bonds results in gating current and conformational change of prestin. Conversely, hyperpolarization forces the Cl^- ion to move into the tunnel to facilitate the binding. Voltage or mechanical force can easily disrupt the anion-π interactions holding the anions and induce ion movement because anion-π interactions are an order of magnitude weaker than ionic interactions. This mechanism may underlie the unique capability of electromechanical and mechanoelectrical (piezoelectric) conversions of prestin with high sensitivity to voltage and mechanical stimulations. The fact that both the anions and the interactions are necessary for the generation of gating current suggests that neither the intracellular anions nor the four tyrosyl residues alone are sufficient for the voltage sensing of prestin. Our model reconciles the two competing models of how prestin works. On one hand, we support the notion that there is no intrinsic voltage sensor (6), the charged residues that can move across the electric field in the same way as that seen in voltage-gated ion channels. On the other hand, we also support the idea that non-covalent bonds between anions and residues are critical for voltage sensing as proposed by Santos-Sacchi and co-workers (15, 16).

Our model has revealed a number of important features unique to prestin. It suggested that prestin contains eight TM-spanning segments with EL3-4, an ICF, and two HP re-entry loops. This is in contrast to previously proposed models containing 10–14 TM regions (10, 23). The structure of our Glt_{Ph}-like model is further divided into an outer shell (TM1–TM6) and an inner core (HP1, HP2, TM7, and TM8). The unique feature of the structure is the ICF, which functionally belongs to the inner core and is neighbored in the sequence by the signature sulfate transport (4) and motile eutherian SLC26A helper motifs (12). These two motifs contribute significantly to the integrity of the unique functional properties of prestin.

Analysis of MD trajectories predicted that four tyrosyl residues (Tyr^{367}, Tyr^{486}, Tyr^{501}, and Tyr^{508}) of the inner core structure are functional components for anion binding (Fig. 8). All four residues participate in weakly polar interactions, which enhance their anion binding capability (28). At the intracellular entrance of the tunnel, Tyr^{508} interacts with residues of ICF, whereas Tyr^{501} interacts with residues that connect HP1 and TM7. ICF has an intrinsic capability to undergo large scale motion (Fig. 2*b*) that may support the entry of Cl^- ions into the tunnel. Thus, the magnitude of NLC was substantially decreased (Fig. 8*a*) when the ICF was deleted. At the top of the tunnel, Tyr^{367} and Tyr^{486} interact with each other, and Tyr^{486} also interacts with Arg^{399}. These two tyrosyl residues together with Arg^{399} and Asp^{485} form an occlusion of the tunnel (Fig. 7).

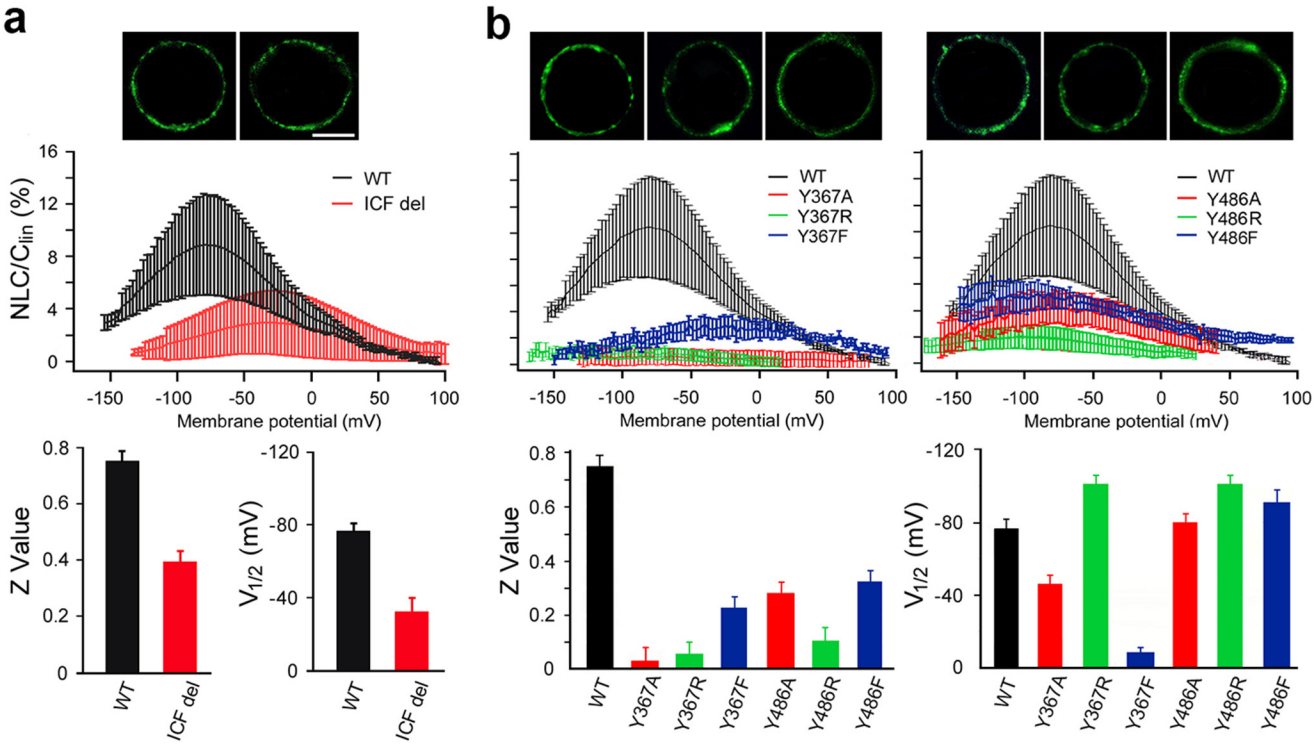

FIGURE 8. **NLC measured from HEK cells transfected with gPres and Tyr^{367} and Tyr^{486} mutant prestins.** *a*, mean ± S.D. (*error bars*) of capacitance-voltage responses of gPres (WT) and mutant prestin without ICF (*ICF del*). NLC was normalized by C_{lin}. Means ± S.D. of $V_{1/2}$ and *z* values obtained from curve fitting the capacitance-voltage responses with the Boltzmann function are presented in the *bottom panels*. The confocal images in the *top panels* show membrane expression of WT and ICF-truncated proteins. *b*, mean ± S.D. (*error bars*) of capacitance-voltage responses of gPres (WT) and prestins with Y367A, Y367R, Y367F, Y486A, Y486R, and Y486F mutations. Means ± S.D. of $V_{1/2}$ and *z* values ($n = 11, 10, 12, 11, 11$, and 12 for Y367A, Y367R, Y367F, Y486A, Y486R, and Y486F, respectively) obtained from curve fitting the capacitance-voltage responses with the Boltzmann function are presented in the *bottom panels*. Examples of membrane expression of the mutant proteins are presented in the *top panels*. From the *left* to *right* are Y367A, Y367R, Y367F, Y486A, Y486R, and Y486F. *Scale bar*, 5 μm.

Thus, complete anion transport through the tunnel will not likely take place.

We indicated that anions can form non-covalent bonds with an aromatic ring of Tyr^{367}, Tyr^{486}, Tyr^{501}, and Tyr^{508} residues through anion-π interactions. Among weakly polar interactions (51), the anion-π interactions are a new type of non-covalent bonds that can stabilize protein structure (27). Through such interactions, inorganic anions (such as Cl^-, Br^-, PO_4^{3-}, and NO_3^-) can bond to aromatic residues in the range of 3.5–4.5 Å and with a 60–90° angle between the vector that connects the anion to the aromatic ring center and the plane of the ring (28). However, the nature and strength of these interactions in proteins are not yet well explored in part because relatively low numbers of such ions are found in the Protein Data Bank. Nevertheless, for Cl^--π interactions, ≤ -10 kcal mol^{-1} interaction energy is predicted by DFT and LMP2 quantum chemical calculations (26) in line with other weakly polar interactions but strong enough to bind anions. Different anions vary in affinity for aromatic rings. This can explain why prestin shows different affinities for different anions (6). For example, the EC_{50} of Cl^- for prestin is 6.3 mM, whereas that for HCO_3^- is 43.6 mM (6).

It is now possible to explain previous experimental results using our three-dimensional model. For example, studies have shown that Val^{499} and Tyr^{501} are critical for NLC and electromotility (55). However, the mechanism of how mutation of these two residues can lead to significant reduction of NLC and outer hair cell motility was unclear. In our model, these two residues, which are located near the junction between the TM8 and the intracellular STAS domain, are positioned at the entrance of the tunnel (Fig. 7). Together with the ICF, Tyr^{501} directly regulates the anion movement in and out of the tunnel. This explains why mutation of these two residues can cause loss of NLC and motility (55). Comparative analysis shows that prestin is the only member of the SLC26A family containing the combination of Tyr^{367}, Arg^{399}, Asp^{485}, and Tyr^{486}, thus making the substrate binding region of prestin unique. Mutation of any of these residues can result in reduction of NLC. Site-directed mutagenesis experiments have demonstrated that R399Q (56) and R399S (23) substitutions significantly altered NLC properties. D485Q mutation, however, did not alter the NLC of prestin (56). These results are consistent with our study. In our three-dimensional model, Arg^{399} directly interacts with Tyr^{486}; therefore, its substitution affects the polarity of the aromatic ring. The D485Q mutation most likely preserves the interaction with Arg^{399} and does not induce structural change. Using the x-ray structure of the bacterial uracil transporter UraA as the template, Gorbunov *et al.* (23) recently proposed a new structural model with 14 TM domains to explain how prestin works. Their model identified different structural components for the voltage-dependent response of prestin. However, the UraA-based model is unable to identify the mechanism for anion transport, voltage sensing, and motor-based movement that facilitates electromotility. Although their study and ours essentially used the same methodologies, the structural components and mechanisms proposed in the two studies are fundamentally different. First of all, in the UraA-based model, residues Ser^{133}–

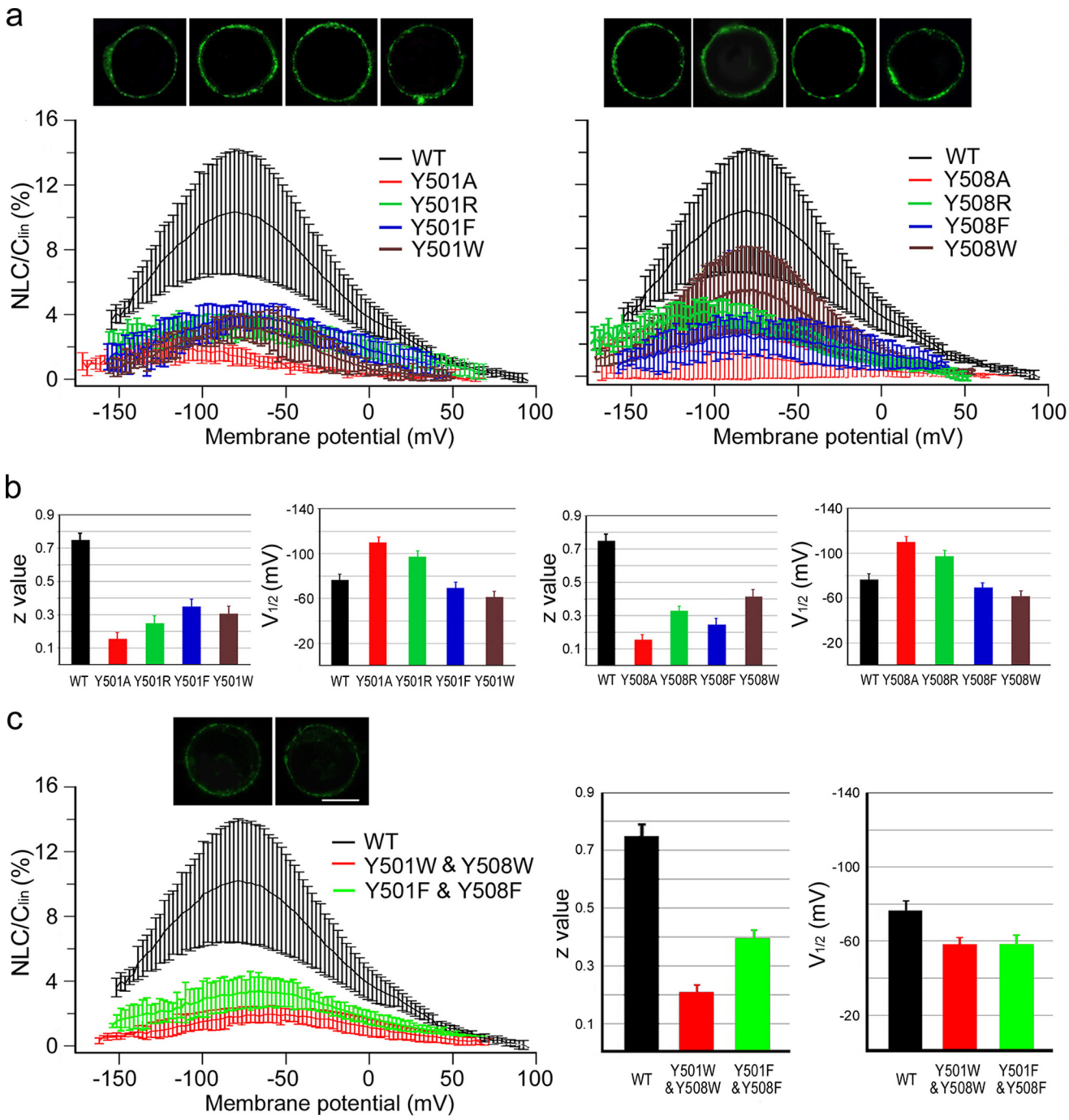

FIGURE 9. **NLC measured from HEK cells transfected with gPres and Tyr^{501} and Tyr^{508} mutant prestins.** *a*, mean ± S.D. (*error bars*) of capacitance-voltage responses measured from prestin with Y501A, Y501R, Y501F, Y501W, Y508A, Y508R, Y508F, and Y508W mutations. Examples of confocal images of membrane expression of the mutant proteins are presented (from the *left* to *right*, Y501A, Y501R, Y501F, Y501W, Y508A, Y508R, Y508F, and Y508W). Capacitance-voltage responses from gPres (WT) were also plotted for comparison. *b*, means ± S.D. (*error bars*) of $V_{1/2}$ and *z* values obtained from the capacitance-voltage responses fitted with the Boltzmann function. $n = 11$ (gPres), 10 (Y501A), 12 (Y501R), 11 (Y501W), 12 (Y501F), 10 (Y508A), 12 (Y508R), 11 (Y508W), 12 (Y508F), 11 (Y508W), and 12 (Y508F). *c*, NLC measured from double mutations at Tyr^{501} and Tyr^{508}. Means ± S.D. (*error bars*) of $V_{1/2}$ and *z* values were obtained from curve fitting with the Boltzmann function. $n = 10$ (Y501W/Y508W) and 12 (Y501F/Y508F). Examples of membrane expression of double mutant proteins are presented. *Scale bar* (applied to all images), 5 μm.

Ile^{156} (identified as the ICF in our model) are in the TM3 region and constitute part of the permeation pathway. Therefore, it is reasonable to expect that the protein would not be able to be expressed in the membrane if a large portion of a TM chain was removed. Our experiment, however, clearly showed that prestin without the ICF was expressed in the membrane. The expression of truncated protein without ICF strongly suggests that these residues are not in the TM region. In addition, the adjacent signature sulfate transport (residues 127–130) (4) and motile eutherian SLC26A helper (residues 158–178) motifs (12) further support the importance of the region encompassing the ICF structure in prestin function. Experiments that alter these motifs by site mutagenesis and/or swapping have demonstrated the functional importance of these two motifs. In the UraA-based model, these are located in the first intracellular and the second extracellular loops, respectively, and as such are

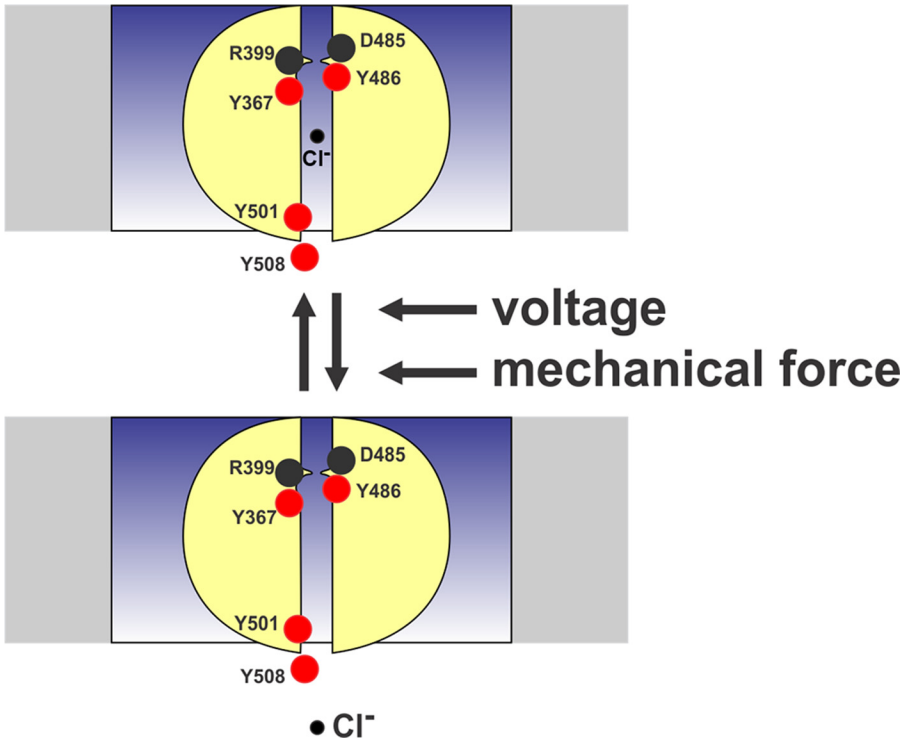

FIGURE 10. **Proposed mechanism mediates unique function of prestin.** Prestin at resting condition has binding sites for Cl^- ions through anion-π interaction. This interaction is much weaker than most of the other non-bonding interactions. The Cl^- ion can easily dissociate from the binding site and generate ion movement during voltage or mechanical stimulation. Binding or disruption of the interactions triggers ion movement (gating current) and subsequent conformational change. The locations of the four tyrosyl residues are indicated by the *red circles*. The sites for Arg^{399} and Asp^{485} and shown by the *gray circles*. The structure of prestin is represented by a shell indicated by the *blue* color-graded *box*, and the core is demarcated by *yellow*.

unlikely to exert a functional impact. This strongly argues against the viability of the UraA-based model proposed by Gorbunov *et al*. (23). Second, our experiments demonstrated that Tyr^{367}, Tyr^{486}, Tyr^{501}, and Tyr^{508} are part of the structural and functional components for anion-π interactions. In the UraA-based model, these residues are either located outside of the proposed anion binding sites or in the shell of the transporter structures. Based on their locations in the UraA-based model, none of the tyrosyl residues should have any impact on the physiological properties of prestin. We clearly showed that they are critical for prestin function. Thus, the UraA-based model is incompatible with our results.

Conceptually, prestin should have at least two essential functional domains: the voltage sensor that detects changes in the membrane potential and the actuator that undergoes a conformational change. Anions need to be translocated across the membrane in response to changes in the transmembrane voltage, moving toward the extracellular surface following hyperpolarization and toward the cytoplasmic side in response to depolarization. As a consequence, this translocation triggers conformational changes in the protein that ultimately alter its surface area in the plane of the plasma membrane. Although our Glt_{Ph}-based model of mammalian prestin does not explain how anion movement can trigger conformational change of the molecule, our new model provides a major step forward in elucidating the structure-function relationships of prestin. Furthermore, although the Glt_{Ph} protein is a trimer and prestin is known to function in homooligomeric form (57, 58), our model does not address the issue of oligomerization. Previous studies have shown that each prestin monomer is mechanically independent in the oligomer (57, 58) and interacts with cytoplasmic partners to facilitate the mechanical response.

Prestin is the only known protein that can respond to mechanical force (deformation) by generating a current (59–61). This piezoelectric property is an order of magnitude better than any man-made piezoelectric crystal (60). None of the existing models so far can explain this. In our model, anions are held by the weak non-covalent bonds inside the tunnel and can easily be expelled by both voltage and mechanical stimulation. Because the bonds are weak, conversion efficiency from mechanical stimulation to current is high. The identification of an anion binding site and the mechanism for high sensitivity to voltage and mechanical stimulations are critical to understanding how prestin works. Our three-dimensional structure can contribute to the design of nanomotors for applications in medicine, protein chemistry, and biomechanical engineering.

Author Contributions—S. L., D. Z. Z. H., and K. W. B. designed the study and wrote the paper. S. L. performed and analyzed MD simulations. H. L. and J. T. performed and analyzed the experiments in Figs. 8 and 9. J. L. P. performed expression of wild type and mutant prestins. M. P. D. H. performed peptide synthesis and experiments in Fig. 4. All authors reviewed the results and approved the final version of the manuscript.

References

1. Dallos, P., Wu, X., Cheatham, M. A., Gao, J., Zheng, J., Anderson, C. T., Jia, S., Wang, X., Cheng, W. H., Sengupta, S., He, D. Z., and Zuo, J. (2008),

Prestin-based outer hair cell motility is necessary for mammalian cochlear amplification. *Neuron* **58,** 333–339
2. Liberman, M. C., Gao, J., He, D. Z., Wu, X., Jia S., and Zuo, J. (2002) Prestin is required for outer hair cell motility and the cochlear amplifier. *Nature* **419,** 300–304
3. Fisher, J. A., Nin, F., Reichenbach, T., Uthaiah, R. C., and Hudspeth, A. J (2012) The spatial pattern of cochlear amplification. *Neuron* **76,** 989–997
4. Brownell, W. E., Bader, C. R., Bertrand, D., and de Ribaupierre, Y. (1985) Evoked mechanical responses of isolated cochlear outer hair cells. *Science* **227,** 194–196
5. Zheng, J., Shen, W., He, D. Z., Long, K. B., Madison, L. D., and Dallos, P. (2000) Prestin is the motor protein of cochlear outer hair cells. *Nature* **405,** 149–155
6. Oliver, D., He, D. Z., Klöcker, N., Ludwig, J., Schulte, U., Waldegger, S., Ruppersberg, J. P., Dallos, P., and Fakler, B. (2001) Intracellular anions as the voltage sensor of prestin, the outer hair cell motor protein. *Science* **292,** 2340–2343
7. Dallos, P., and Fakler, B. (2002) Prestin, a new type of motor protein. *Nat. Rev. Mol. Cell Biol.* **3,** 104–111
8. Mount, D. B., and Romero, M. F (2004) The SLC26 gene family of multifunctional anion exchangers. *Pflugers Arch.* **447,** 710–721
9. Ohana, E., Yang, D., Shcheynikov, N., and Muallem, S. (2009) Diverse transport modes by the solute carrier 26 family of anion transporters. *J. Physiol.* **587,** 2179–2185
10. He, D. Z., Lovas, S., Ai, Y., Li, Y., and Beisel, K. (2014) Prestin at year 14: progress and prospect. *Hear. Res.* **311,** 25–35
11. Schaechinger, T. J., Gorbunov, D., Halaszovich, C. R., Moser, T., Kügler, S., Fakler, B., and Oliver, D. (2011) A synthetic prestin reveals protein domains and molecular operation of outer hair cell piezoelectricity. *EMBO J.* **30,** 2793–2804
12. Tan, X., Pecka, J. L., Tang, J., Lovas, S., Beisel, K. W., and He, D. Z. (2012) An eleven-amino-acid motif is a structural adaptation that facilitates motor capability of eutherian prestin. *J. Cell Sci.* **125,** 1039–1047
13. Tan, X., Pecka, J. L., Tang, J., Okoruwa, O. E., Zhang, Q., Beisel, K. W., and He, D. Z. (2011) From zebrafish to mammal: functional evolution of prestin, the motor protein of cochlear outer hair cells. *J. Neurophysiol.* **105,** 36–44
14. Tang, J., Pecka, J. L., Tan, X., Beisel, K. W., and He, D. Z (2011) Engineered pendrin protein, an anion transporter and molecular motor. *J. Biol. Chem.* **286,** 31014–31021
15. Rybalchenko, V., and Santos-Sacchi, J. (2003) in *Biophysics of the Cochlea: from Molecules to Models* (Gummer, A., ed) pp. 116–126, World Scientific Publishing, Singapore
16. Song, L., and Santos-Sacchi, J. (2010) Conformational state-dependent anion binding in prestin: evidence for allosteric modulation. *Biophys. J.* **98,** 371–376
17. Chang A. B., Lin, R., Studley, W. K., Tran, C. V., and Saier, M. H., Jr. (2004) Phylogeny as a guide to structure and function of membrane transport proteins. *Mol. Membr. Biol.* **21,** 171–181
18. Wong, F. H., Chen, J. S., Reddy, V., Day, J. L., Shlykov, M. A., Wakabayashi S. T., and Saier, M. H., Jr. (2012) The amino acid-polyamine-organocation superfamily. *J. Mol. Microbiol. Biotechnol.* **22,** 105–113
19. Vastermark, A., Wollwage, S., Houle, M. E., Rio, R., and Saier, M. H., Jr. (2014) Expansion of the APC superfamily of secondary carriers. *Proteins* **82,** 2797–2811
20. Västermark, Å., and Saier, M. H., Jr. (2014) Evolutionary relationship between 5+5 and 7+7 inverted repeat folds within the amino acid-polyamine-organocation superfamily. *Proteins* **82,** 336–346
21. Yamaguchi, T., Ikeda, Y., Abe, Y., Kuma, H., Kang, D., Hamasaki, N., and Hirai, T. (2010) Structure of the membrane domain of human erythrocyte anion exchanger 1 revealed by electron crystallography. *J. Mol. Biol.* **397,** 179–189
22. Lu, F., Li, S., Jiang, Y., Jiang, J., Fan, H., Lu, G., Deng, D., Dang, S., Zhang, X., Wang, J., and Yan, N. (2011) Structure and mechanism of the uracil transporter UraA. *Nature* **472,** 243–246
23. Gorbunov, D., Sturlese, M., Nies, F., Kluge, M., Bellanda, M., Battistutta, R., and Oliver, D. (2014) Molecular architecture and the structural basis for anion interaction in prestin and SLC26 transporters. *Nat. Commun.* **5,** 3622
24. Lovas, S., He, D. Z., Hatfield, M. P. D., Pecka, J. L., Okoruwa, O. E., Tang, J., Jia, S., and Beisel, K. W. (2011) in *Proceedings of the 22nd American Peptide Symposium* (Lebl, M., ed) pp. 120–121, American Peptide Society, Albuquerque, NM
25. Frontera, A., Gamez, P., Mascal, M., Mooibroek, T. J., and Reedijk, J. (2011) Putting anion-π interactions into perspective. *Angew. Chem. Int. Ed. Engl.* **50,** 9564–9583
26. Jones, G. J., Robertazzi, A., and Platts, J. A. (2013) Efficient and accurate theoretical methods to investigate anion-π interactions in protein model structures. *J. Phys. Chem. B* **117,** 3315–3322
27. Philip, V., Harris, J., Adams, R., Nguyen, D., Spiers, J., Baudry, J., Howell, E. E., and Hinde, R. J. (2011) A survey of aspartate-phenylalanine and glutamate-phenylalanine interactions in the protein data bank: searching for anion-π pairs. *Biochemistry* **50,** 2939–2950
28. Robertazzi, A., Krull, F., Knapp, E.-W., and Gamez, P. (2011) Recent advances in anion-π interactions. *CrystEngComm* **13,** 3293–3300
29. Okoruwa, O. E., Weston, M. D., Sanjeevi, D. C., Millemon, A. R., Fritzsch, B., Hallworth, R., and Beisel, K. W. (2008) Evolutionary insights into the unique electromotility motor of mammalian outer hair cells. *Evol. Dev.* **10,** 300–315
30. Lobley, A., Sadowski, M. I., and Jones, D. T. (2009) pGenTHREADER and pDomTHREADER: new methods for improved protein fold recognition and superfamily discrimination. *Bioinformatics* **25,** 1761–1767
31. Krieger, E., Joo, K., Lee, J., Lee, J., Raman, S., Thompson, J., Tyka, M., Baker, D., and Karplus, K. (2009) Improving physical realism, stereochemistry, and side-chain accuracy in homology modeling: four approaches that performed well in CASP8. *Proteins* **77,** Suppl. 9, 114–122
32. Bowers, K. J., Chow, E., Xu, H., Dror, R. O., Eastwood, M. P., Gregersen, B. A., Klepeis, J. L., Kolossváry, I., Moraes, M. A., Sacerdoti, F. D., Salmon, J. K., Shan, Y., and Shaw, D. E. (2006) in *Proceedings of the ACM/IEEE Conference on Supercomputing (SC06), Tampa, Florida, November 11–17, 2006*, Article 84, Association for Computing Machinery, New York
33. Kaminski, G., Friesner, R. A., Tirado-Rives, J., and Jorgensen, W. L. (2001) Evaluation and reparametrization of the OPLS-AA force field for proteins via comparison with accurate quantum chemical calculations on peptides. *J. Phys. Chem. B* **105,** 6474–6487
34. Tuckerman, M., Berne, B. J., and Martyna, G. J. (1992) Reversible multiple time scale molecular dynamics. *J. Chem. Phys.* **97,** 1990–2001
35. Lippert, R. A., Bowers, K. J., Dror, R. O., Eastwood, M. P., Gregersen, B. A., Klepeis, J. L., Kolossvary, I., and Shaw, D. E. (2007) A common, avoidable source of error in molecular dynamics integrators. *J. Chem. Phys.* **126,** 046101
36. Pronk, S., Páll, S., Schulz, R., Larsson, P., Bjelkmar, P., Apostolov, R., Shirts, M. R., Smith, J. C., Kasson, P. M., van der Spoel, D., Hess, B., and Lindahl, E. (2013) GROMACS 4.5: a high-throughput and highly parallel open source molecular simulation toolkit. *Bioinformatics* **29,** 845–854
37. Daura, X., Gademann, K., Jaun, B., Seebach, D., van Gunsteren, W. F., and Mark, A. E (1999) Peptide folding: when simulation meets experiment. *Angew. Chem. Int. Ed.* **38,** 236–240
38. Kabsch, W., and Sander, C. (1983) Dictionary of protein secondary structure: pattern recognition of hydrogen-bonded and geometrical features. *Biopolymers* **22,** 2577–2637
39. Palermo, N. Y., Thomas, P., Murphy, R. F., and Lovas, S. (2012) Hexapeptide fragment of carcinoembryonic antigen which acts as an agonist of heterogeneous ribonucleoprotein M. *J. Pept. Sci.* **18,** 252–260
40. Szendrei, G. I., Fabian, H., Mantsch, H. H., Lovas, S., Nyéki, O., Schön, I., and Otvos, L., Jr. (1994) Aspartate-bond isomerization affects the major conformations of synthetic peptides. *Eur. J. Biochem.* **226,** 917–924
41. Sreerama, N., and Woody, R. W (2000) Estimation of protein secondary structure from circular dichroism spectra: comparison of CONTIN, SELCON, and CDSSTR methods with an expanded reference set. *Anal. Biochem.* **287,** 252–260
42. Lobley, A., Whitmore, L., and Wallace, B. A. (2002) DICHROWEB: an interactive website for the analysis of protein secondary structure from circular dichroism spectra. *Bioinformatics* **18,** 211–212
43. Santos-Sacchi, J., Shen, W., Zheng, J., and Dallos, P. (2001) Effects of membrane potential and tension on prestin, the outer hair cell lateral mem-

brane motor protein. *J. Physiol.* **531,** 661–666
44. Ashmore, J. F. (1989) in Cochlear Mechanisms: Structure, Function, and Models (Wilson, J. P., and Kemp, D. T., eds) pp. 107–114, Plenum Publishing, New York
45. Santos-Sacchi, J. (1989) Asymmetry in voltage-dependent movements of isolated outer hair cells from the organ of Corti. *J. Neurosci.* **9,** 2954–2962
46. Zheng, J., Long, K. B., Shen, W., Madison, L. D., and Dallos, P. (2001) Prestin topology: localization of protein epitopes in relation to the plasma membrane. *Neuroreport* **12,** 1929–1935
47. Ohana, E., Shcheynikov, N., Yang, D., So, I., and Muallem, S. (2011) Determinants of coupled transport and uncoupled current by the electrogenic SLC26 transporters. *J. Gen. Physiol.* **137,** 239–251
48. Sousounis, K., Haney, C. E., Cao, J., Sunchu, B., and Tsonis, P. A. (2012) Conservation of the three-dimensional structure in non-homologous or unrelated proteins. *Hum. Genomics* **6,** 10
49. Illergård, K., Ardell, D. H., and Elofsson, A. (2009) Structure is three to ten times more conserved than sequence—a study of structural response in protein cores. *Proteins* **77,** 499–508
50. Shrivastava, I. H., Jiang, J., Amara, S. G., and Bahar, I. (2008) Time-resolved mechanism of extracellular gate opening and substrate binding in a glutamate transporter. *J. Biol. Chem.* **283,** 28680–28690
51. Csontos, J., Palermo, N. Y., Murphy, R. F., and Lovas, S. (2008) Calculation of weakly polar interaction energies in polypeptides using density functional and local Moller-Plesset perturbation theory. *J. Comput. Chem.* **29,** 1344–1352
52. Nishio, M., Umezawa, Y., Fantini, J., Weiss, M. S., and Chakrabarti, P. (2014) CH-π hydrogen bonds in biological macromolecules. *Phys. Chem. Chem. Phys.* **16,** 12648–12683
53. Chourasia, M., Sastry, G. M., and Sastry, G. N (2011) Aromatic-Aromatic Interactions Database, A(2)ID: an analysis of aromatic π-networks in proteins. *Int. J. Biol. Macromol.* **48,** 540–552
54. Naider, F. (2007) Synthesis, biosynthesis, and characterization of transmembrane domains of a G protein-coupled receptor. *Methods Mol. Biol.* **386,** 95–121
55. Homma, K., Duan, C., Zheng, J., Cheatham, M. A., and Dallos, P. (2013) The V499G/Y501H mutation impairs prestin's fast motor kinetics and has significance for defining functional independence of individual prestin subunits. *J. Biol. Chem.* **288,** 2452–2463
56. Bai, J.-P., Surguchev, A., Montoya, S., Aronson, P. S., Santos-Sacchi, J., and Navaratnam, D. (2009) Prestin's anion transport and voltage-sensing capabilities are independent. *Biophys. J.* **96,** 3179–3186
57. Wang, X., Yang, S., Jia, S., and He, D. Z. (2010) Prestin forms oligomer with four mechanically independent subunits. *Brain Res.* **1333,** 28–35
58. Hallworth, R., and Nichols, M. G. (2012) Prestin in HEK cells is an obligate tetramer. *J. Neurophysiol.* **107,** 5–11
59. Gale, J. E., and Ashmore, J. F. (1994) Charge displacement induced by rapid stretch in the basolateral membrane of the guinea-pig outer hair cell. *Proc. Biol. Sci.* **255,** 243–249
60. Dong, X., Ehrenstein, D., and Iwasa, K. H. (2000) Fluctuation of motor charge in the lateral membrane of the cochlear outer hair cell. *Biophys. J.* **79,** 1876–1882
61. He, D. Z., Jia, S., Sato, T., Zuo, J., Andrade, L. R., Riordan, G. P., and Kachar, B. (2010) Prestin function and the structure of the lateral membrane of outer hair cells. *Cytoskeleton* **67,** 43–55